Molecular Mechanism of Crystalline-to-Amorphous Conversion of Pharmaceutical Solids from ^{19}F Magic Angle Spinning NMR

Xingyu Lu[1,§], Chengbin Huang[1,§], Mingyue Li[1,§], Daniel Skomski[1], Wei Xu[1], Lian Yu[2], Stephen R. Byrn[3], Allen C. Templeton[1], and Yongchao Su[1,3,4,*]

[1]Pharmaceutical Sciences, Merck & Co., Inc., Kenilworth, NJ 07033, United States

[2] School of Pharmacy and Department of Chemistry, University of Wisconsin−Madison, Madison, WI 53705, United States

[3] Department of Industrial and Physical Pharmacy, College of Pharmacy, Purdue University, IN 47907, United States

[4] Division of Molecular Pharmaceutics and Drug Delivery, College of Pharmacy, The University of Texas at Austin, Austin, Texas 78712, United States

Revised for *J. Phys. Chem. B*

April 15th, 2020

[§]X. L., C. H. and M. L. have equal contribution.

* Corresponding author: Y. S.: yongchao.su@merck.com

Table of Content (TOC) Figure

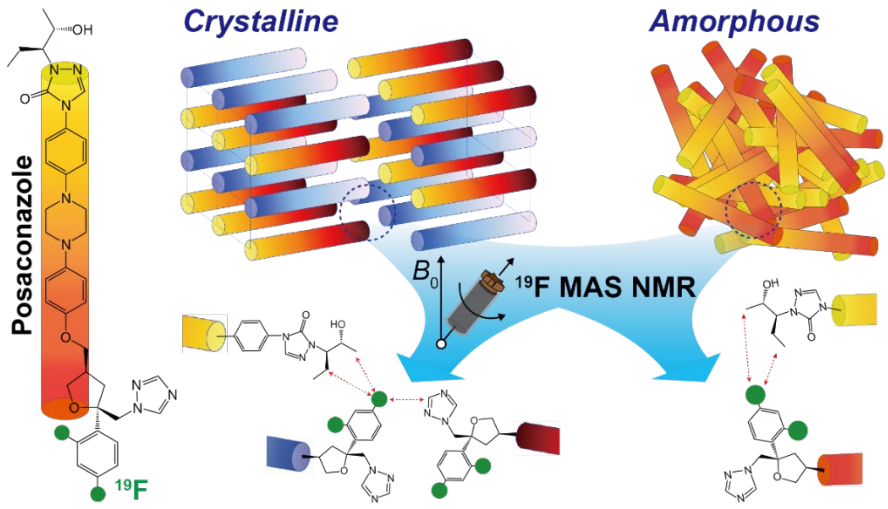

Abstract

Crystalline and amorphous materials usually possess distinct physiochemical properties due to major variations in long-range as well as local molecular packing. An enhanced fundamental knowledge of the molecular details of crystalline-to-amorphous interconversions is necessary to correlate the intermolecular structure to material properties and functions. While crystal structures can be readily obtained by X-ray crystallography, the microstructure of amorphous materials has rarely been explored due to a lack of high-resolution techniques capable of probing local molecular structures. Moreover, there is increasing interest in understanding the molecular nature of amorphous solids in pharmaceutical sciences due to the widespread utilization of amorphous active pharmaceutical ingredients (APIs) in pharmaceutical development for solubility and bioavailability enhancement. In this study, we explore multi-dimensional ^{13}C and ^{19}F magic angle spinning (MAS) NMR spectroscopy to study molecular packing of amorphous posaconazole (POSA) in conjunction with the crystalline counterpart. Utilizing methods integrating homo-nuclear and heteronuclear ^{1}H, ^{13}C, and ^{19}F correlation spectroscopy and atomic ^{19}F-to-^{13}C distance measurements, we identified the major differences in molecular packing between crystalline and amorphous POSA. The intermolecular "head-to-head" interaction along the molecule's major axis, as well as the "head-to-tail" molecular packing perpendicular to the major axis in POSA crystals, were recapitulated by MAS NMR. Furthermore, critical inter-molecular distances in the crystal lattice were determined. Most importantly, the "head-to-tail" contact of two neighboring molecules was found to be preserved in amorphous POSA, suggesting localized molecular order, whereas crucial interactions for "head-to-head" packing are absent in the amorphous form resulting in long-range disorder. Our study, likely one of the first documented examples, provide molecular-level structural details to understand the molecular mechanism of crystalline-to-amorphous conversion of fluorine-containing drug substances occurring in drug processing and development and establish a high-resolution experimental protocol for investigating amorphous materials.

1. Introduction

Organic solids, commonly categorized in their supramolecular structures as crystalline or amorphous materials, have numerous applications ranging from pharmaceutics[1, 2] to electronics[3, 4]. Active pharmaceutical ingredients (APIs) have traditionally been formulated as solids in their crystalline form in many pharmaceutical products. However, solid state APIs can adopt different molecular structures and packing arrangements in the crystal lattice, a phenomenon known as polymorphism[5]. The consistency of molecular packing of API crystals is crucial for ensuring the delivery of drug products of the same physicochemical properties such as solubility, stability, and manufacturability. More recently, amorphous forms of APIs are increasingly recognized for delivering poorly water-soluble drug substances due to improved solubility and bioavailability compared to crystalline counterparts[6]. In the industrial production of amorphous solids, three-dimensional (3D) molecular packing in crystals is purposefully disrupted generating solids possessing long-range disorder. Analogously to crystal polymorphism, amorphous solids might exist in different phases, referred as polyamorphism. Polyamorphism has been reported for ice[7], triphenyl phosphite (TPP)[8], *n*-butanol[9] and D-mannitol[10, 11]. Even though amorphous solids have been generally known for being disordered, localized molecular packing and intermolecular contacts have not been fully explored. Such information is important for understanding the stability of amorphous solids manufactured by different methods. It is known that amorphous solids are unstable in their pure form and have a strong tendency to recrystallize. To characterize structural details of amorphous materials, many techniques have been utilized, for example Infrared spectroscopy (IR)[11, 12,12], Raman spectroscopy[10], and X-ray scattering[7, 8, 11, 13,13], whereas these methods lack the spatial resolution to probe fine details of the 3D molecular packing of amorphous systems. Neutron and X-ray pair function analysis of glassy materials can delineate intermolecular distances from intra-molecular atom-atom correlations, thereby revealing the weakening of inter-molecular correlations in the glassy form of several drug molecules[13]. However, the analysis is complicated by broad peaks of the amorphous drugs, spectral interferences from pharmaceutical excipients, and detailed interaction information was still missing. It remains a technical challenge to explore inter-molecular packing of crystalline and amorphous organic solids.

Solid-state nuclear magnetic resonance spectroscopy (ssNMR) has emerged as an extremely powerful analytical technique for characterization of pharmaceutical solids, including polymorphism, structure determination, and interactions[14-24]. The development of NMR crystallography enables validation, refinement, and *de novo* structure determination of both crystalline and microcrystalline solids[25-44]. NMR crystallography is a hybrid approach that integrates magic angle spinning (MAS) NMR with molecular modeling, quantum calculations, and other techniques such as powder X-ray diffraction (PXRD) to solve molecular structures of small molecules[45-49]. Potential structure candidates are generated based on atomic

connectivity and further optimized upon theoretical energy minimization[50]. Density functional theory (DFT) calculations of NMR parameters of these structural candidates can correlate with experimental NMR observables to determine the correct structure with the lowest root-mean-square (rms) error. Most commonly, chemical shift tensors and proton spin diffusion (PSD) data have been used for structure determination. Harper and coworkers published a series of investigations by measuring and modeling accurate chemical shift tensors of ^{13}C and ^{15}N atoms in organic solids to refine their crystal structures[40-44]. An integrated method of PSD data in conjunction with ^{1}H and ^{13}C chemical shifts and DFT chemical shift calculations has been used to determine thymol structure with high-resolution[36]. The *de novo* crystal structure of a drug molecule as large as 422 g/mol is determined by a similar protocol[33]. To probe for molecular packing and intermolecular interactions, Brown and coworkers developed an approach of using ^{1}H DQ (double quantum) build-up rate and maximum intensities for quantitative analysis of intra- and inter-molecular ^{1}H-^{1}H proximities in gamma-indomethacin with the support of density matrix simulations[51]. Moreover, the NMR chemical shift calculation of the full crystal and an isolated molecule yield chemical shift changes due to hydrogen bonding and CH-pi interactions which are formed in a crystal lattice[51, 52]. In addition, distance constrains have been applied to NMR crystallography in determining molecular configuration with ^{13}C and ^{15}N isotopic labeling[53, 54], in which ^{13}C-^{15}N rotational-echo double-resonance (REDOR) hetero-nuclear dipolar recoupling measurements are utilized[55]. REDOR is one of the most reliable NMR methods to measure distances by recoupling dipolar interactions. Due to the low natural abundance and low gyromagnetic ratio of ^{15}N in organic solids, ^{15}N-^{13}C distance constrains are not commonly used in NMR crystallography due to the low sensitivity. For a subset of molecules containing ^{31}P and/or ^{19}F, one potential solution to this issue is to measure distances between these 100% natural abundance isotopes and ^{13}C. Rienstra and coworkers demonstrated applicability of ^{13}C-^{31}P REDOR for refinement of candidate crystal structures, and showed that the ^{13}C-^{31}P distance is exceptionally informative for NMR crystallography[27]. Since about 30% of FDA-approved small molecule drugs contain fluorine, a distance measurement method based on ^{19}F-^{13}C REDOR could have many potential applications in pharmaceutical sciences, such as structure determination of APIs and intermolecular interaction studies of API-API and API-excipients. For its high sensitivity, ^{19}F MAS NMR has been demonstrated as a powerful technique for probing molecular details of small molecules and biomolecules.

^{19}F NMR spectroscopy has been widely employed for quantification[56, 57], studying molecular interactions[24, 58, 59], assessing molecular mobility[60, 61], identifying molecular orientations[62], and structural characterizations of fluorine-containing solids [63-67]. Fluorine chemical shift tensor measurements combined with computational calculations provide insight into local electronic environments around ^{19}F-sites[59,62,62, 63, 68, 69]. In addition, ^{19}F-^{1}H and ^{19}F-^{13}C correlations are sensitive probes of molecular conformation and

interactions in bulk materials and pharmaceutical solid dispersions[56-59, 63-65]. Qualitative and quantitative analyses of poximities of ^{19}F to other nuclei have been widely utilized to probe molecular structures. 2D ^{13}C-^{19}F hetero-nuclear correlation spectroscopy (HETCOR) was applied to determine the hetero-nuclear proximity between avagacestat and a polymer and can probe fluorine-carbon distances of up to 8 Å[70]. High-resolution 3D ssNMR techniques developed by Lu et al. can simultaneously provide ^{1}H-^{1}H, ^{1}H-^{19}F, and ^{19}F-^{19}F correlations of the crystalline aprepitant in the formulated drug product[71]. ^{19}F-^{19}F correlations capable of probing interatomic distances of the order of 2 nm in large protein assemblies have been reported by Wang et al.[72]. Quantatitive distance measurements between ^{19}F and other nucleri such as ^{1}H, ^{15}N, and ^{13}C have been demonstrated in biomolecules by REDOR[73-75]. For example, ^{1}H-^{19}F distances of a peptide were determined in model peptide solids using a REDOR sequence[73]. Intramolecular ^{13}C-^{19}F dipolar coupling of fluroine-substitied cholesterol embeded in lipid bilayer was determined by a ^{13}C-^{19}F REDOR experiment. The reduced dipolar coupling compared to a rigid bond implicates internal molecular mobility[62]. Shcherbakov et al. employed 1D and 2D REDOR to measure ^{13}C-^{19}F distances of up to 10 Å in proteins[76] at MAS frequencies of 25 kHz to 40 kHz, which could potentially be used for structure determination. Polenova and coworkers have demonstrated the importance of fast MAS frequencies of 40 kHz - 60 kHz for consistently establishing long-range ^{19}F-^{19}F correlations[72]. They also reported a combination of ^{19}F fast MAS and DNP that resulted in a 100-fold signal enhancement on HIV-1 capsid protein assemblies, which enables the detection of long-range intra- and inter-molecular ^{19}F-^{13}C correlations inaccessible by conventional experiments[71]. Therefore, ^{13}C-^{19}F REDOR technique has great potential for simultaneously measuring intra- and inter-molecular distances in fluroine-containing pharmaceutical solids in both crystalline and amorphous forms.

In this study, we develop an approach employing ^{19}F MAS NMR in combination with ^{1}H, ^{15}N, and ^{13}C NMR techniques to probe long-range order in crystalline solids and molecular packing of amorphous solids using a model compound posaconazole (POSA). POSA is the active pharmaceutical ingredient (API) of a second-generation triazole antifungal drug (Noxafil, Merck & Co., Inc., Kenilworth, NJ, USA). It is a rod-like molecule which contains rich chemical functional groups on both ends of the molecular structure, including difluorophenyl and triazole rings at one end and a triazolone ring, a hydroxyl group, and aliphatic carbons at the other end, as shown in **Figure 1A**. It has been recently reported that the glass form of POSA, prepared via vapor deposition, exhibits aligned smectic packing. [77, 78]. A combination of ^{13}C chemical shifts, ^{19}F CSA, and ^{13}C-^{19}F transfer measurements allows for qualitative assessment of molecular structure and packing in the unit cell. Intra- and inter-molecular distances of ^{19}F to ^{13}C were obtained by ^{13}C-^{19}F REDOR experiments and confirmed by the crystal structure. Furthermore, we determined intra- and inter-molecular

^{13}C-^{19}F distances in the amorphous forms of POSA prepared by melt-quenching, which are critical for identifying major differences in molecular packing during crystalline-to-amorphous interconversions.

2. Experimental Section

2.1. Materials

Crystalline posaconazole (POSA) was provided by Merck & Co., Inc., Kenilworth, NJ, USA. Isotopically $^{13}C/^{15}N$ labeled POSA [IUPAC: 4-(4-(4-(4-(((3S,4R)-4-((1H-1,2,4-triazol-1-yl)methyl)-4-(2,4-difluorophenyl)tetrahydrofuran-3-yl)methoxy)phenyl)piperazin-1-yl)phenyl)-2-((2S,3R)-2-hydroxypentan-3-yl)-2,4-dihydro-3H-1,2,4-triazol-3-one-5-^{13}C1,2-^{15}N2] was synthesized for site-specific investigations by ssNMR. The ^{13}C and ^{15}N-enriched sites are labeled in red in **Figure 2C**. Amorphous POSA was prepared by cooling POSA melt to room temperature via contact with an aluminum block. Following gentle grinding in a mortar and pestle, amorphous POSA powder was stored in a desiccator at room temperature prior to ssNMR measurements. The nature of crystalline POSA and amorphous POSA were confirmed by powder XRD patterns shown in **Figure S1**.

2.2. Solid-State Nuclear Magnetic Resonance (ssNMR) Spectroscopy

Experiments were performed using a Bruker Avance III HD 400 triple-resonance spectrometer operating at ^{1}H frequency of 400.13 MHz in the Biopharmaceutical NMR Laboratory (BNL) of Preclinical Development, MRL, Merck & Co., Inc. West Point, PA 19486, USA. All experiments were carried out at 298 K and a MAS frequency of 12 kHz. Experimental data were processed in Bruker TopSpin software. ^{13}C and ^{19}F spectra were obtained with a Bruker 4 mm triple-resonance HFX MAS probe tuned to ^{1}H, ^{19}F, and ^{13}C frequencies. ^{13}C and ^{1}H spectra were obtained with the HXY MAS probe in double-resonance mode tuned to ^{1}H and ^{13}C frequencies. 1D $^{1}H \rightarrow {}^{13}C$ and $^{19}F \rightarrow {}^{13}C$ cross-polarization (CP) transfers were performed at a radio frequency (rf) strength of 80-100 kHz; the power level was ramped linearly during the contact time over a depth of 15 to 20 kHz on the ^{1}H or ^{19}F channel to enhance CP efficiency, respectively. ^{1}H and ^{19}F hetero-nuclear decoupling of 100 kHz was performed using SPINAL-64 pulse sequence during acquisition. ^{13}C-edited spectra were obtained using standard CP combined with polarization inversion and simultaneous phase inversion (CPpispi) pulse sequence[79]. ^{1}H and ^{13}C spectra were referenced to tetramethylsilane (TMS). ^{19}F spectra were referenced to Teflon at -122 ppm. In 1D ^{13}C-^{19}F REDOR experiments, ^{13}C 180° pulse of 8 μs was applied to refocus the ^{13}C chemical shift during the REODR mixing period. The ^{19}F rf-field strength was 83.3 kHz in the REDOR period. REDOR simulations were performed using the SIMPSON software. ^{19}F and ^{13}C pulse lengths were matched to experiments in the simulation. Multi-spin simulation considering two ^{19}F and two carbons are tested and found to give similar fittings to a

three-spin (two ^{19}F and one ^{13}C) model. ^{19}F chemical shift anisotropy (CSA) values are measured at 12 kHz MAS and included in simulation of REDOR dephasing curve.

3. Results

We have previously identified the interesting crystalline-to-amorphous conversion of POSA upon compression and proposed interparticulate interactions as a mechanism of amorphization[57]. Amorphous posaconazole (POSA) is the preferred form to its crystalline counterpart in the formulated drug product due to improved solubility and bioavailability. Therefore, it is critical to understand the molecular mechanism of POSA's crystalline-to-amorphous conversation. The goal of this study is to understand key structural differences of crystalline and amorphous solids underlying changes in physical properties of POSA using ssNMR. We firstly combine chemical shift analysis and ^{1}H-^{13}C, ^{19}F-^{19}F,^{19}F-^{1}H, and ^{19}F-^{13}C correlation and transfer experiments to probe molecular differences of crystalline and amorphous POSA. ^{13}C-^{19}F REDOR measurements are then implemented for quantitative depiction of molecular packing by determining intermolecular distances. These results have successfully derived the first structural model of molecular packing of amorphous POSA.

3.1. Chemical Shift Assignments of Crystalline and Amorphous Posaconazole

It is often challenging to fully assign the resonances of small molecules in pharmaceutical NMR studies due to the low sensitivity from natural abundance species. To provide site-specific investigations in this study, we aim to provide unambiguous peak assignment of POSA. The 1D ^{13}C CP MAS spectrum of crystalline POSA acquired with a 2-ms contact time has 26 peaks of 37 inequivalent carbons exhibiting significant peak overlapping, as shown in **Figure 1B**. By referencing the solution NMR chemical shifts[80] and following the previously published protocol for assigning ssNMR resonances[24], we have successfully identified all ^{13}C peaks. For example, to differentiate carbon CH_n groups (n = 0 - 3) of different multiplicities, the 1D ^{13}C-edited spectra in **Figures 1C** and **1D** were acquired to selectively show carbons with the desired multiplicity and therefore greatly facilitate resonance assignments in the peak-overlapping area. A quaternary carbon (C34) from an aromatic group and a CH group (C23) from the triazole ring both have a ^{13}C resonance of 149.7 ppm, and appear as one combined peak in the 1D ^{13}C CP MAS. They appear as two separate peaks in a quaternary carbon selective CP spectrum in **Figure 1C** and a CH-selected CP spectrum in **Figure 1D**. ^{13}C-edited spectra also allowed us to assign the broad peak around 128 ppm to a combination of one CH group (C19) and two quaternary carbons (C14, C37). Moreover, ^{19}F-bonded ^{13}C has peak splitting due to the hetero-nuclear dipolar coupling (**Figure 1F**, top). Therefore, it is helpful to utilize ^{19}F decoupling for assigning these carbons. Two 1D ^{13}C CP experiments in **Figure 1F** were acquired with the application of ^{19}F decoupling during acquisition (on) and without (off). Due to the decoupling of the strong

^{19}F-^{13}C dipolar interaction, ^{19}F covalently-bonded carbons show significant sensitivity improvement and therefore new isolated peaks are assigned to fluorinated carbons C15 and C17.

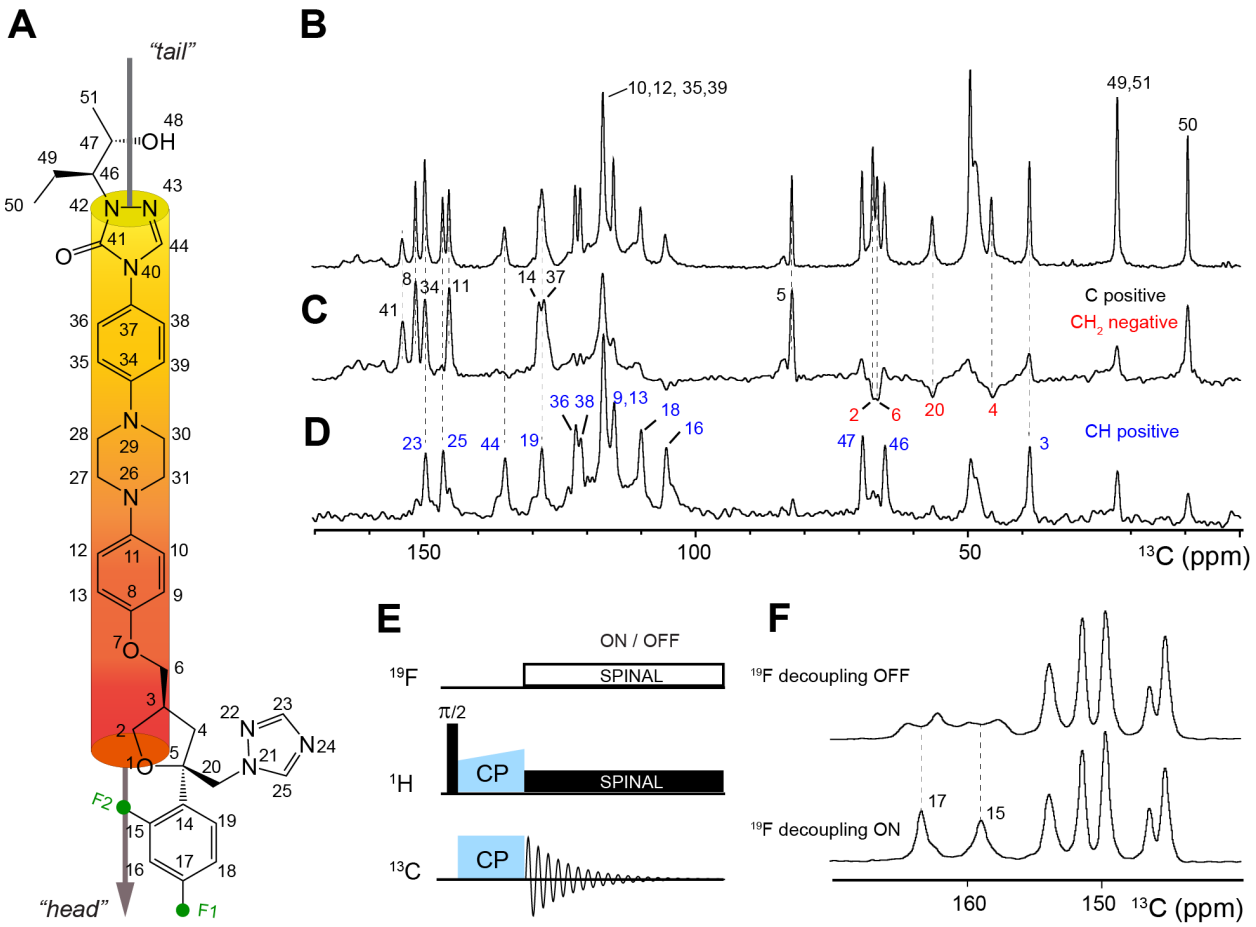

Figure 1. Molecular structure and one-dimensional (1D) ^{13}C- and ^{19}F-edited MAS NMR spectra of crystalline POSA. (A) Schematic structure of POSA with carbon numbering labeled. The arrow indicates a hypothetical "head-to-tail" molecular axis; (B) 1D ^{1}H→^{13}C CP spectrum with 2 ms contact time; (C) 1D ^{13}C-edited CP spectrum with negative -CH_2 peaks (red), positive -C peaks (black), and -CH peaks vanished; (D) 1D ^{13}C-edited CP spectrum selective for -CH peaks (blue). -CH_2 and -C peaks are vanished; (E) Pulse sequence of ^{13}C CP MAS with (on) and without (off) ^{19}F hetero-nuclear decoupling; (F) ^{13}C CP MAS spectra of fluorine-bonded carbons recorded with (bottom) and without (top) ^{19}F hetero-nuclear decoupling. All spectra were acquired at a MAS frequency of 12 kHz.

Preliminary ^{13}C chemical shift assignments obtained based on the above-mentioned 1D experiments were further refined and confirmed with a 2D ^{13}C-^{1}H HETCOR experiment, in which the addition of ^{1}H dimension correlates ^{13}C and ^{1}H in proximity and assists with identifying peaks in crowed regions with an improved resolution. **Figure 2A** shows site-specific, one-bond ^{13}C-^{1}H correlations of crystalline POSA acquired with a short contact time of 100 µs. For isolated carbon peaks, the chemical shift of covalently bonded protons was also assigned. The assignment of ^{13}C and ^{15}N resonances at the

aliphatic end of POSA was further assisted by a ^{15}N-^{13}C correlation experiment. C44, N42, and N43 in the triazolone ring were ^{13}C and ^{15}N isotopically enriched, and therefore allow for the direct observation of one-bond and two-bond ^{15}N-^{13}C correlations as shown in **Figure 2B**. Note that for materials of natural abundance, the detection of ^{15}N-^{13}C correlations is challenging due to extremely low sensitivity and may be possible using DNP-enhanced NMR[16]. More importantly, correlations of natural abundance C41 and C46 with labeled N42 were also observed and assigned in the spectrum. The unambiguous assignment of C41 and C46 is important for the study of intermolecular packing of crystalline POSA, which will be discussed in a later section. We applied these experimental protocols to both crystalline and amorphous POSA and obtained full ^{13}C chemical shift assignments (summarized in **Table 1)**. A plot of chemical shift differences for each carbon site in the two forms is shown in **Figure S2**. Chemical shift differences are observed and may suggest changes in molecular packing between the crystalline and amorphous forms. For example, C2, C4, C5, and C6 show chemical shift changes > 2 ppm and are mostly aliphatic carbons localized close to difluorophenyl and triazolone rings of the molecule, which exhibit rich intra- and inter-molecular contacts in the crystalline form. It is possible that reorientation of the aromatic rings in the amorphous form causes chemical shift changes in these carbon sites.

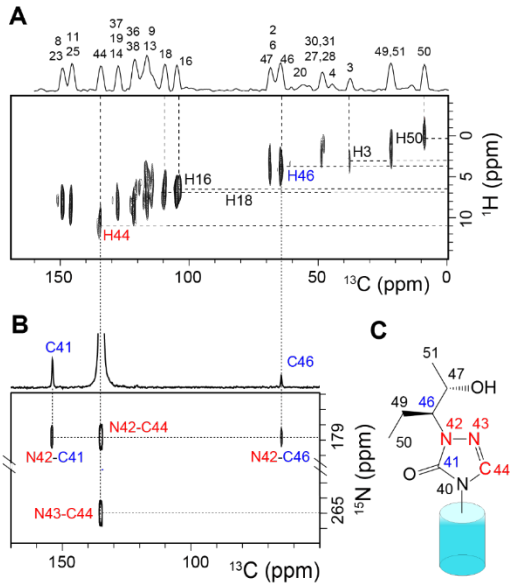

Figure 2. (A) 2D ^{1}H-^{13}C HETCOR spectrum of crystalline POSA with a short contact time of 100 μs, acquired at MAS frequency of 12 kHz. ^{13}C assignments are labeled in the 1D projection displayed on top of the 2D spectrum. (B) 1D (top) and 2D (bottom) ^{15}N-^{13}C correlation spectra of crystalline POSA showing one-bond and two-bond correlations. Note the correlation between natural abundance C41 and C46 and isotopically labeled N42 are highlighted. (C) A representative molecular structure of the aliphatic end of POSA, where isotopically labeled N42, N43, and C44 are highlighted in red.

Table 1. ^{13}C chemical shifts of crystalline and amorphous POSA.

^{13}C No.	Crystalline POSA	Amorphous POSA
2	67.2	70.8
3	38.4	39.7
4	45.4	37.0
5	82.2	84.4
6	66.5	70.8
8	151.4	151.5
9	115.0	114.5
10	116.9	116.7
11	145.3	146.3
12	116.9	116.7
13	115.0	114.5
14	128.5	127.0
15	158.8	159.2
16	105.4	104.9
17	163.2	163.5
18	110.0	111.9
19	128.2	127.5
20	56.3	56.2
23	149.7	151.1
25	146.4	145.8
27	49.3	49.8
28	48.2	49.8
30	48.2	49.8
31	49.3	49.8
34	149.7	151.0
35	116.9	116.7
36	122.0	122.1
37	127.9	127.0
38	121.1	122.1
39	116.9	116.7
41	153.9	153.4
44	135.1	134.9
46	65.1	63.7
47	69.2	68.9
49	22.2	24.0
50	9.2	11.1
51	22.2	21.3

3.2. Intramolecular and Intermolecular Proximities in Crystalline and Amorphous Solids

^{13}C-^{1}H proximities in Crystalline Posaconazole

Bond lengths and interatomic distances of crystalline solids are valuable inputs for structural determination. Herein, we utilized 2D ^{1}H-^{13}C hetero-nuclear correlation (HETCOR) to probe interatomic proximities in crystalline POSA in a semi-quantitative manner. This analysis focuses on the ^{13}C-enriched C44 of crystalline POSA, based on its high spectral sensitivity. A series of 2D ^{13}C-^{1}H HETCOR spectra with mixing times ranging from 100 μs to 3000 μs were acquired and shown in **Figure 3A**, and plots of peak intensity versus contact times for C44-H44 one-bond and C44- H36/38 multi-bond transfers were extracted and shown in **Figure 3B**. The build-up curve of ^{1}H-^{13}C HETCOR magnetization transfer reflects the atomic distance between carbon and protons. C44-H44 and C44-H36 distances are 1.7 Å and 3.5 Å, respectively, as measured in X-ray single crystal structure[81]. The one-bond C44-H44 build-up curve quickly reaches its maximum at 100 μs mixing while the 4-bond C44-H36/38 build-up curve is still growing at 2000 μs mixing. Therefore, the 2D ^{1}H-^{13}C HETCOR signal build-up curve can serve as a semi-qualitative method for probing ^{13}C-^{1}H proximity. It is worth noting that H44 is involved in intra- and intermolecular contacts in the crystalline lattice [81], which may impact its NMR relaxation profile and the CP transfer to C44.

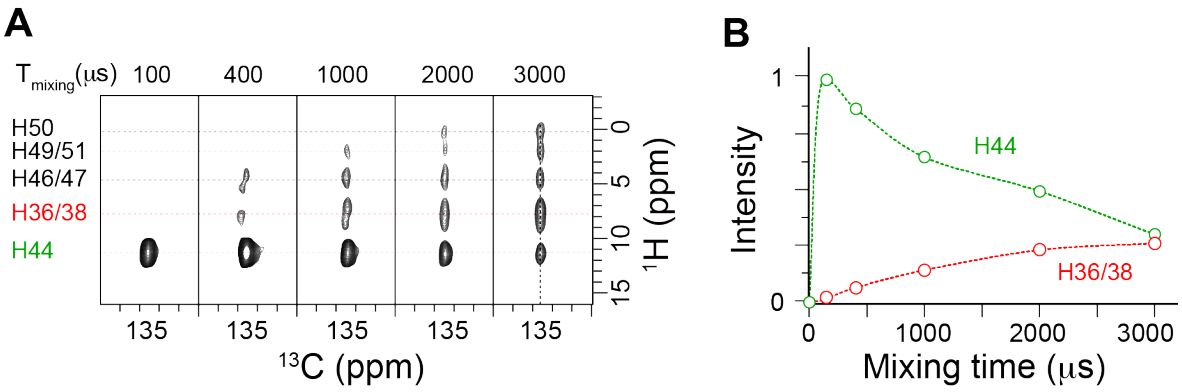

Figure 3. (A) 2D ^{13}C-^{1}H HETCOR spectra showing correlations between ^{13}C-labled C44 and protons (1-5 bonds). Contact times are 100, 400, 1000, 2000, and 3000 μs from left to right, respectively; (B) Plots of peak intensity as a function of mixing times extracted from 2D ^{13}C-^{1}H HETCOR spectra in (A).

^{19}F-^{19}F and ^{19}F-^{1}H Proximities in Crystalline and Amorphous Posaconazole

In this section, ^{19}F NMR is utilized to explore the molecular structure and inter-molecular packing of POSA in crystalline and amorphous forms. 2D ^{19}F-^{19}F and ^{19}F-^{1}H experiments are highly sensitive methods to characterize fluorinated molecules and provide rich chemical shift, bond distance, and molecular contact information. The para-fluorine (F1) located in a more isolated chemical environment is more shielded than the ortho-fluorine (F2) and thus is assigned to a lower chemical shift of -113.4 ppm. The 2D ^{19}F-^{19}F RFDR (Radio-Frequency Driven Recoupling) correlation spectrum in **Figure 4A** shows intra-molecular correlations between F1 and F2. The 2D ^{19}F-^{1}H HETCOR spectrum with 100 μs mixing time in

Figure 4B correlate both fluorine sites with aromatic protons at around 7 ppm in the same ring. Interestingly, para-fluorine (F1) shows an additional contact with aliphatic protons around 2 ppm, which is preliminarily assigned to H50/H49. Since the intra-molecular distance of C50 and F1 is approximately 19 Å based on the POSA single-crystal structure[81] (shown in **Figure 4E**), correlations of F1 and aliphatic ^{1}H in this 2D spectrum are very likely due to inter-molecular contacts between the difluorophenyl ring of one molecule and the aliphatic carbons of another molecule as shown in **Figure 4D**. Moreover, the 2D ^{19}F-^{1}H HETCOR spectrum in **Figure 4C** recorded with a 1 ms contact time reveals that F2 is also close to aliphatic protons from other molecules, but is further away than F1. Similarly, such inter-molecular contacts are retained in amorphous POSA by the observation of ^{19}F correlations with aliphatic protons in a similar experiment (**Figure 4D**). Very interestingly, these results suggest that a close inter-molecular proximity in crystalline POSA is retained in its amorphous form.

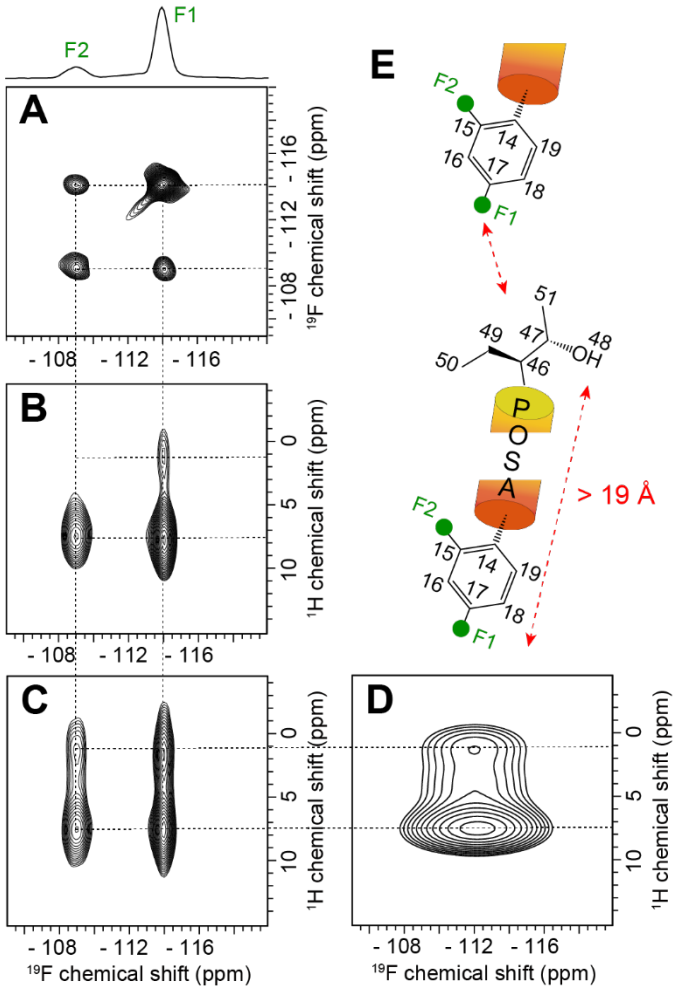

Figure 4. 2D ^{1}H-^{1}H and ^{1}H-^{19}F correlation spectra of crystalline and amorphous POSA. (A) 2D ^{19}F-^{19}F RFDR spectrum of crystalline POSA with a 1 ms contact time showing an intramolecular correlation between fluorine atoms; 2D ^{1}H-^{19}F HETCOR spectra of crystalline POSA with 100 µs (B) and 1 ms (C)

contact times; (D) 2D ^{1}H-^{19}F HETCOR of amorphous POSA using a 1 ms contact time. All spectra were acquired at a MAS frequency of 12 kHz. (E) A hypothetical model showing intra- and inter-molecular ^{19}F-^{1}H contacts in crystalline POSA.

Intra- and Intermolecular ^{19}F-^{13}C Distance Measurements in Crystalline and Amorphous Posaconazole.

^{19}F-^{13}C correlations further elucidate spatial connectivities in POSA molecules thanks to the complete assignments of ^{19}F and ^{13}C atoms. For example, chemical shift assignments of two fluorine atoms and covalently bonded carbons in crystalline POSA were further corroborated by a 2D ^{19}F-^{13}C HETCOR correlation spectrum shown in **Figure 5A**. This heteronuclear correlation experiment has been recently developed to faciliate the resonance assignment of fluorinated proteins.[82] With a short mixing time of 400 μs and no ^{1}H decoupling, peaks correlating fluorine and covalently bonded carbon atoms are observed in the spectrum. To probe ^{19}F and ^{13}C contacts at a longer distance, 1D CP transfers with ^{1}H decoupling at short and long mixing times are probed and shown in **Figure 5B**. The spectral comparison to crystalline POSA (top two spectra in **Figure 5B**) shows intra-molecular (carbon numbers in purple) and inter-molecular (carbon numbers in red) ^{19}F-^{13}C correlations. The C23-F correlation suggests a "head-to-head" packing between two molecules. Other carbons including C49, C50, and C51 also exhibit inter-molecular correlations with fluorine, indicating an "head-to-tail" packing. Both packing models are observed in the single-crystal X-ray structure. It is worthy of note that the "head-to-tail" packing has also been demonstrated in the ^{19}F-^{1}H correlation in **Figure 4D**. 1D spectra of amorphous POSA acquired at short and long mixing times are shown in the bottom two spectra in **Figure 5B**. Identical carbon resonances from the intra-molecular ^{19}F-^{13}C transfer are observed (carbon numbers in purple). While C49, C50, and C51 peaks show up in the long CP spectrum (the bottom spectrum in **Figure 5B**), the C23 peak does not appear. This suggest the "head-to-head" packing has disappeared in the amorphous state of POSA, but the "head-to-tail" contact is still retained. **Figure 5C** demonstrates a model of both "head-to-head" and "head-to-tail" packings in crystalline POSA.

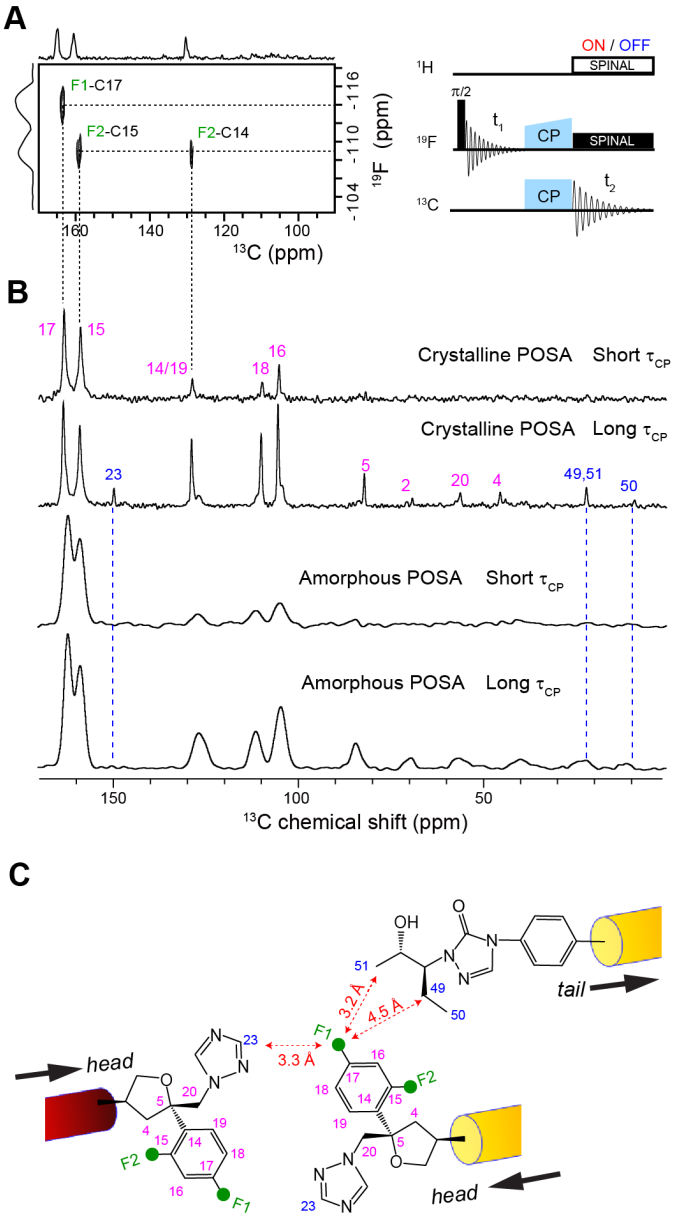

Figure 5. Intra- and inter-molecular ^{13}C-^{19}F contacts from 1D and 2D MAS NMR correlations. (A) 2D ^{13}C-^{19}F HETCOR spectrum with a short 400 µs contact time and without proton decoupling during acquisition (for identifying directly bonded ^{19}F-^{13}C spin pairs). The pulse sequence with and without proton decoupling during acquisition is shown on the right; (B) 1D ^{19}F→^{13}C CP spectra of crystalline (top two) and amorphous (bottom two) POSA with short (400 µs) and long (2000 µs) contact times. (C) A representative model showing inter-molecular contacts of crystalline POSA. Carbons involved in intra- and inter-molecular ^{19}F-^{13}C contacts are labeled in purple and blue, respectively. Representative distances are obtained from the X-ray crystallography structure[81].

To obtain quantitative information of structural restraints, we utilized rotational-echo double-resonance (REDOR) experiments to measure ^{13}C-^{19}F atomic distances. Such experiments measure inter-atomic distances by recoupling hetero-nuclear dipolar coupling of a spin pair[55]. ^{13}C-^{19}F REDOR curves of

amorphous POSA and simulations are shown in **Figure 6** and the distances determined are summarized in **Table 2**, together with corresponding distances in crystalline POSA measured by ssNMR and single-crystal X-ray diffraction[81]. The distance restraints in amorphous POSA provide likely the first documented case of Å-level characterization of pharmaceutical glass.

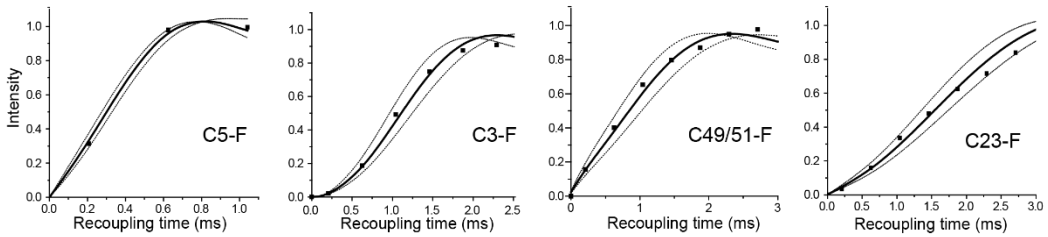

Figure 6. ^{13}C-^{19}F REDOR measurements of carbon-fluorine distances in amorphous POSA. C5 and C3 are representative examples of intra-molecular contacts with fluorine. C49/51 and C23 are inter-molecular contacts with fluorine. The comparisons of ^{13}C-^{19}F distances in crystalline and amorphous POSA are included in **Figure S3** and **Table 2**.

The comparison of ^{13}C-^{19}F distances in crystalline POSA by ssNMR and single-crystal X-ray diffraction measurements has been reported in our previous study and confirmed the robustness of ^{13}C-^{19}F REDOR experiments. Briefly, taking C5-F distance measurements as an example (**Figure S3**), the curve fitting shows a distance of 2.7 ± 0.1 Å. This agrees well with the shortest distance of 2.8 Å among a few C5-F1 and C5-F2 contacts (**Table 2**). The weaker ^{13}C-^{19}F dipolar coupling is truncated by the strong coupling of the C-F pair at a shorter proximity and therefore does not impact the fitting (multi-spin fitting results not shown). The short intra-molecular distances (C5-F and C3-F) remain the same for crystalline and amorphous POSA, suggesting the absence of large-scale molecular conformational changes at one end of the molecule between the two forms. The inter-molecular ^{13}C-^{19}F distances between aliphatic carbons (C49/51) and fluorine atoms are also comparable in crystalline and amorphous POSA (**Figure S3**). This quantitative data further confirms the inter-molecular "head-to-tail" contact previously identified in **Figure 4E** and **5B**. Interestingly, a major ^{13}C-^{19}F distance difference is identified at C23. C23-F shows a short distance of 3.3 ± 0.1 Å in crystalline POSA, identifying the close inter-molecular C23-F1 and C23-F2 contacts. In comparison, it becomes 6.2 ± 0.3 Å in the amorphous form, which agrees well with the intra-molecular C23-F1 and C23-F2 distances. The absence of a short C23-F distance suggests the "head-to-head" packing in crystalline form disappears in the amorphous form.

Table 2. Comparison of intra- and inter-molecular ^{13}C-^{19}F distances in crystalline and amorphous POSA determined by ssNMR and single-crystal X-ray diffraction[81].

C and F spin pairs	XRD (Å) [81]		ssNMR (Å)	
	crystalline		crystalline	amorphous
	Inter	intra		
C3-F1	6.7	7.3	4.3 ± 0.3	4.3 ± 0.3
C3-F2	7.3	4.5		
C5-F1	4.6	5.7	2.7 ± 0.1	2.9 ± 0.1
C5-F2	5.4	2.8		
C49/51-F1	4.5/3.2	20.5/22.2	4.3 ± 0.3	4.5 ± 0.3
C49/51-F2	4.5/4.9	21.1/22.3		
C50-F1	5.7	19.7	5.0 ± 0.4	4.5 ± 0.2
C50-F2	5.2	20.5		
C23-F1	3.3	6.7	3.3 ± 0.1	6.2 ± 0.3
C23-F2	3.9	5.6		

3.3. Probing Molecular Interactions in Crystalline and Amorphous POSA from ^{19}F Chemical Shift Anisotropy (δ_{CSA}) Measurements

According to Shcherbakov *et al.*, when ^{19}F chemical shift anisotropy (CSA) exceeds the MAS frequency by two-fold, the REDOR dephasing curve deviates from its ideal shape and its variance depends on the CSA value[76]. Therefore, fluorine CSA values are measured and included in simulations of the REDOR dephasing curve at a regular MAS rate. In addition, ^{19}F CSA is also a sensitive NMR parameter for changes of structure, interactions, and molecular dynamics,[83-85] and thus can be utilized to probe the difference between crystalline and amorphous POSA. For these two reasons, we measured δ_{CSA} of two fluorine sites in both crystalline and amorphous forms. The deconvolution of ^{19}F spectra are shown in **Figure 7A** and **7B**, chemical shift tensors extracted by lineshape fitting are summarized in **Table 3,** and corresponding principle components (δ_{11}, δ_{22}, and δ_{33}) are included in **Table S1**. Among these values, F1 in both forms has a smaller absolute δ_{CSA} than F2, suggesting a relatively more flexibility. This can be explained by F1 being isolated from other chemical groups, and its motion is less hindered. A previous study reported δ_{CSA} values of 47-63 ppm in crystalline fluorosubstituted tryptophans[85]. Our results show relatively large δ_{CSA} values of two fluorine atoms in both crystalline and amorphous forms, suggesting a relative high rigidity. This finding might be explained by the similar "head-to-tail" contacts in both forms. This inter-molecular interaction between the difluorophenyl ring and aliphatic end present a locally-packed structure. However, the amorphous form exhibits a profound lack of long-range order, as seem from the disappearance of the "head-to-head" packing. It results in molecular mobility, which may rationalize the slightly smaller CSA of amorphous POSA. The measurement of ^{19}F CSA can be further improved at a lower MAS frequency.

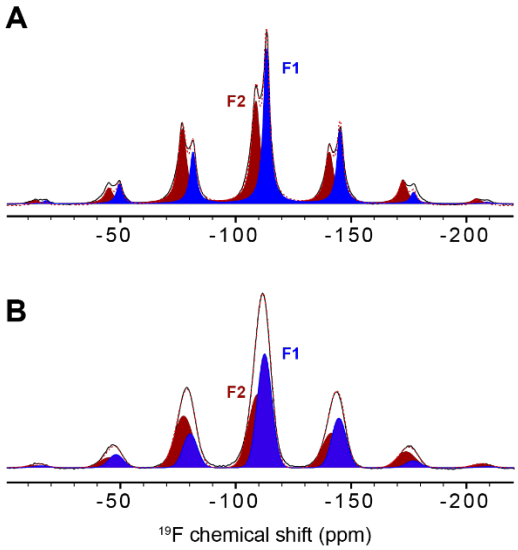

Figure 7. ^{19}F chemical shift tensors of (A) crystalline and (B) amorphous POSA. The deconvolutions of two fluorine sites are shown as red and blue areas.

Table 3. ^{19}F isotropic and anisotropic chemical shift parameters of crystalline and amorphous POSA including isotropic chemical shift (δ_{iso}) and chemical shift anisotropy (δ_{CSA}).

	^{19}F sites	δ_{iso} (ppm)	δ_{CSA} (ppm)
Crystalline	F1	-113.4	66.2
	F2	-108.8	-78.1
Amorphous	F1	-112.8	62.5
	F2	-109.9	-75.0

4. Discussion

Head-to-head and Head-to-tail Packing of Crystalline and Amorphous Posaconazole

POSA molecules form "head-to-tail" and "head-to-head" molecular packings in the crystal lattice as shown in the crystal structure in **Figure 8A**, which is stabilized by rich hydrogen bonding interactions[81]. In particular, the hydroxyl group at the aliphatic end acts as a hydrogen bond acceptor for a triazole group at the difluorophenyl end of an antiparallel molecule; the triazole group also acts as a hydrogen bond donor to the hydroxyl group of another antiparallel molecule, leading to a "head-to-tail" packing structure. In addition, the C-H⋯O=C hydrogen bond between triazolone groups is responsible to the parallel molecules in a direction perpendicular to the molecular major axis (**Figure 1A**). Moreover, there is also "head-to-head" interaction of the same end along the molecule's major axis. The difluorophenyl group acts a hydrogen bond donor to the triazole group. The C-H bond *ortho* to both fluorine atoms is directed to the triazole to form C-H⋯N-C hydrogen bonding. By having these interactions, "head-to-tail" chains are linked to form

2D planes. We simplify the "head-to-tail" and "head-to-head" packing schemes in POSA crystals in a schematic model shown in **Figure 8B**.

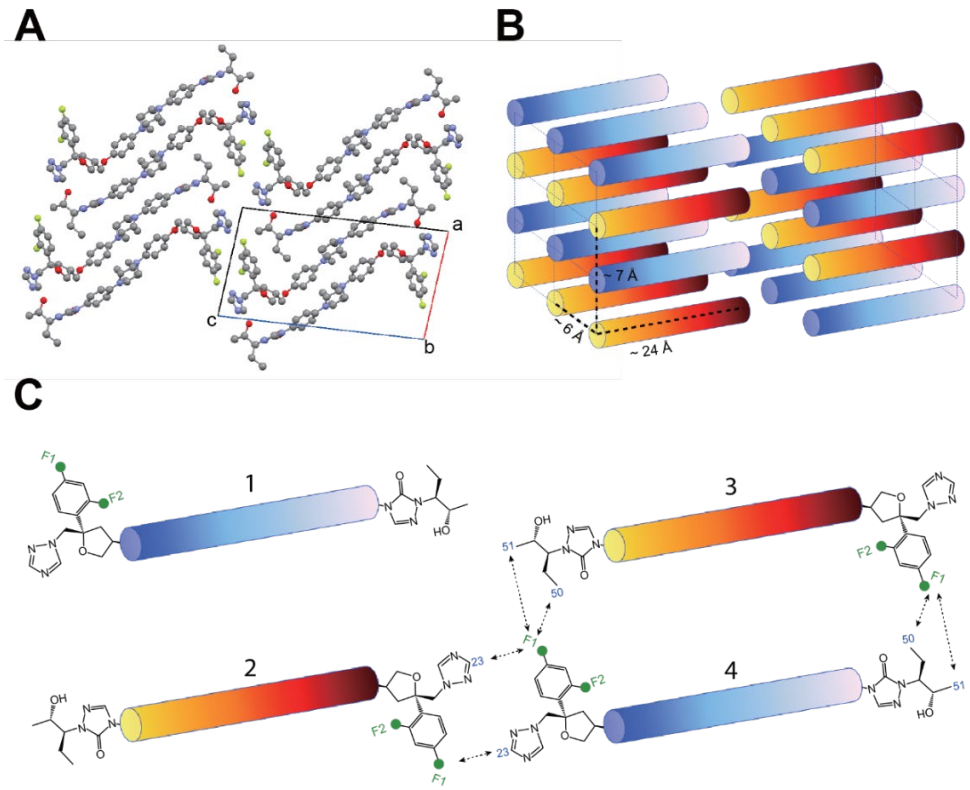

Figure 8. Molecular packings of crystalline POSA. (A) View along the *b* axis of the crystal structure. (B) A schematic view of inter-molecular packing in the crystal lattice. (C) Hypothetic models of "head-to-head" and "head-to-tail" packing of POSA molecules generated based on ssNMR data. "Head-to-head" packing is presented by molecules 2 and 4; molecules 3 and 4 represent "head-to-tail" packing.

These packing structures have also been identified based on three sets of ssNMR results. The inter-molecular correlation between the difluorophenyl ring and aliphatic chains in **Figure 4E** suggests the "head-to-tail" packing. The ^{19}F-^{13}C magnetization transfer in **Figure 5B** identifies the close proximity between C23 and fluorine atoms and between C49, C50, and C51 and fluorine atoms, confirming the "head-to-head" and "head-to-tail" packing, respectively. Finally, REDOR has identified the short C49/51-F and C23-F distances in **Figure 6** and **Table 2**, as the atomic-level distance restraints identify the two kinds of packing. These results successfully recapitulate key features of molecular packing pattern in POSA and construct a molecular packing model of crystalline POSA in **Figure 8C**, which features the "head-to-head" and "head-to-tail" alignments.

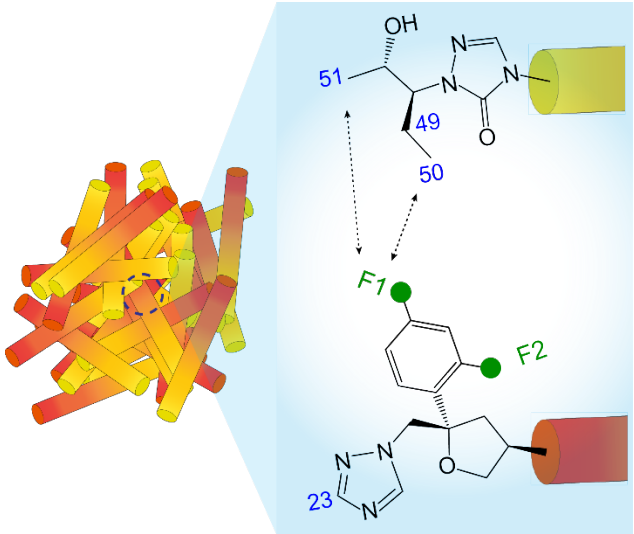

Figure 9. Schematic model of a "head-to-tail" packing in amorphous POSA.

Furthermore, we investigated molecular packing of amorphous POSA, of which the microstructure had not been explored in detail previously. Differences in molecular packing upon amorphous formation are clearly indicated by chemical shift perturbations, changes of anisotropic chemical shifts, differences in ^{13}C-^{19}F correlation spectra, and inter-molecular distance changes. Significant chemical shift changes of a few carbon sites at the difluorophenyl end suggest variations in molecular packing upon amorphization (Table 1). The difluorophenyl ring also shows slightly increased mobility in amorphous POSA than the crystalline counterpart indicated by relatively reduced absolute ^{19}F CSA (**Table 3**). Enhanced mobility is consistent with a general understanding that amorphous solids are often associated with increased molecular dynamics, due to the lack of long-range packing. Site-specific changes in molecular packing were further observed in ^{13}C-^{19}F correlation experiments in **Figure 5B**. With most intra-molecular correlations conserved in crystalline and amorphous POSA solids, inter-molecular magnetization transfers from opposite ends of the molecule are also retained due to the "head-to-tail" packing. However, "head-to-head" packing resulting from inter-molecular interactions of the difluorophenyl ends of neighboring molecules in a crystal lattice is missing in the amorphous form, as identified by semi-quantitative ^{19}F-^{13}C CP experiments (**Figure 5B**) and quantitative REDOR measurement (**Table 2**). These structural restraints help to construct a schematic model in **Figure 9**, which uncover a lack of long-range order and a tendency towards local "head-to-tail" packing.

Typically, glasses were regarded as homogeneous disordered materials, when prepared by melt-quenching or liquid-cooling. The previous study by Ediger and coworkers[77] utilized Infrared spectroscopy (IR) and ellipsometry to explore molecular orientation inside POSA glasses. In this likely the first study on

molecular packing of amorphous POSA, the order parameter S_z from IR, indicating the average molecular orientation of the long molecular axis, and birefringence from ellipsometry, calculated from a uniaxially anisotropic Cauchy dispersion model and the refractive indices, were utilized. It was found that molecules are oriented for the POSA glasses produced by physical vapor deposition (PVD). Such amorphous POSA were deposited into films at different substrate temperatures, and were found to have different molecular orientations. At near-glass transition temperature T_g, the deposited POSA glasses show the "nematic-like" structure, in which molecules are mostly neighbored to one another and perpendicular to the interface of POSA films and the substrate upon deposition. It is worth noting that molecules are assumed to be centrosymmetric in their study and have possibilities of both parallel and antiparallel packings. This "nematic-like" packing structure is proposed to be supported by the surface equilibrium and the molecule's rod-like shape.[77] Interestingly, no preferential orientation was detected for the amorphous POSA film obtained by melt-quenching in IR and ellipsometry measurements. Different from ellipsometry and IR which focus on macroscopically preferential orientation, ssNMR determines inter-molecular structure by quantifying homo- or hetero-nuclear distances at atomic level. Semi-quantitative ^{19}F-^{13}C correlations and quantitative distance restraints in our study uncover a "head-to-tail molecular packing in melt-quenching POSA glasses. This offers one of the few examples identifying inter-molecular packing in amorphous materials at atomic level. The "head-to-tail" packing of two POSA molecules in glasses, as identified by the highly similar C49-F, C50-F and C51-F distances in crystalline and amorphous POSA, is not surprising if considering the strong hydrogen bond acceptor-donor pairs at the opposite ends of the molecule as described in Etter's rules, *e.g.* 2-aminopyrimidine and carboxylic acid[86]. It is worthy of note that the ssNMR does not require specifically prepared amorphous materials, *e.g.* glass condensed on the substrate surface via PVD, and thus can analyze samples produced from major ASD processes. These structural findings are critical to understanding the relationship between microstructure of amorphous materials and physical properties and thus guiding the application of amorphous materials in the pharmaceutical industry. More distance restraints in future studies, e.g. those which offer identifications of intermolecular contacts across the entire lengthy of the molecule, can further uncover the full packing structure of the neighboring molecules in amorphous POSA.

MAS NMR as a High-Resolution Technique for Probing Molecular Details of Amorphous Materials

It is of great scientific interest to understand fundamental physiochemical mechanism of amorphous natures for its utilization in numerous technologies and applications. For example, the pharmaceutical excipient of D-mannitol has two amorphous phases, namely SCL and Phase X, which own different glass transition temperatures, free energies, densities, and hydrogen bonds.[10, 11] Zhu *et al.* utilized flotation method to quantify density and found that Phase X is 2.1% less dense than SCL. Furthermore, the difference

in Near IR (NIR) spectra of D-mannitol has been observed at 6198 cm^{-1} and 6820 cm^{-1}, which corresponds to stronger and weaker hydrogen bonds respectively. NIR spectra suggest that Phase X has the strong hydrogen bonds in comparison to SCL. Clearly, D-mannitol polyamorphism appears to arise from the competing demands of hydrogen bonds and packing efficiency. Besides, variations in molecular packing from crystalline to amorphous materials usually result in noticeably different physiochemical properties such as dissolution rate and stability[12, 87]. For this reason, solid dosages may be formulated in amorphous form for enhanced bioavailability. It becomes critical to understand the change of molecular packing in crystalline form during thermal or mechanical amorphization processes. Therefore, it is important to develop methods for investigating the difference of molecular packing between crystalline and amorphous forms to better understand the structure-property relationships of amorphous materials. While single-crystal X-ray diffraction has been a prominent technique in solving 3D crystal structure, characterization of molecular structure and molecular packing of amorphous materials remains a challenging task. Conventional methods, such as IR, Raman spectroscopy, and powder X-ray diffraction, have been utilized to explore the molecular details of amorphous solids; however, none of them can provide distance constrains for understanding amorphous molecular packing at atomic level.

In recent years, ssNMR has been utilized as a powerful tool to gain structural insights on structure, interactions, and dynamics of pharmaceutical materials at molecular or atomic resolution. There have been an extensive amount of studies focusing on crystalline drug substance and products. Recently, the structural investigation on amorphous pharmaceuticals has attracted increased attention due to the emerging drug products formulated from the amorphous form. For example, our previous study has identified rich molecular interactions between POSA and different polymers, HPMCAS and HPMCP, in amorphous formulations by utilizing 2D ^{1}H-^{13}C, ^{19}F-^{13}C, ^{15}N-^{13}C, and ^{19}F-^{1}H correlation experiments[59]. Mistry *et al.* investigated the formation of API-polymer hydrogen bonding in amorphous solid dispersions of ketoconazole and poly(acrylic acid) using ^{13}C and ^{15}N MAS NMR[88]. Munson and coworkers reported the various hydrogen-bonding species of amorphous indomethacin through self-interactions by deconvolution of ^{13}C CPMAS spectra of the isotopically labeled carboxylic acid region, and investigated the role of polymers in the disruption of API-API hydrogen bonding[17]. Tatton *el al.* applied 2D ^{14}N-^{1}H dipolar hetero-nuclear multiple-quantum coherence (HMQC) experiments to demonstrate the presence of intermolecular hydrogen bonding interactions in an amorphous dispersion of nicotinamide palmitic acid[89]. These studies serve as successful examples investigating molecular interactions in the multicomponent drug products. However, the fundamental mechanism of structural change of drug substances, *i.e.*, crystalline-to-amorphous conversation has rarely been explored at molecular resolution. In this study, we utilize ^{19}F as a sensitive probe to study the structure of a fluorine-containing small-molecule drug POSA and characterize

long- and short-range order to understand the different packing in crystalline and amorphous forms. The ^{19}F-based techniques help to overcome the challenge of low sensitivity of natural abundance materials and provides site-specific structural information. Various 2D ^{19}F-^{19}F, ^{19}F-^{1}H, and ^{19}F-^{13}C correlation experiments provide qualitative and semi-quantitative identification of molecular structures. Using ^{13}C-^{19}F REDOR experiments, we are able to determine both intra- and inter-molecular ^{13}C-^{19}F distances of up to 6.2 Å. These distance constraints are important for deriving the high-resolution inter-molecular packing model of molecules in amorphous forms, which is extremely challenging for other routine techniques. Moreover, cutting-edge ssNMR techniques including dynamic nuclear polarization (DNP) and ultrafast MAS (up to 110 kHz spinning) have been remarkably advanced in the past few years[90]. We have previous developed a sample preparation protocol to utilize DNP for in-situ characterization of POSA amorphous formulations[16]. Most recently, Emsley and coworkers have made an applauding progress on ^{19}F DNP and obtained an enhancement of 100[91]. Besides, spectra acquired at ultrafast MAS have shown largely enhanced ^{19}F sensitivity and resolution, which enables 3D experiments to characterize drug products at natural abundance[92]. Therefore, ^{19}F MAS NMR characterization of pharmaceutical materials will be significantly benefited if combined with DNP and ultrafast MAS. While more than 30% of FDA-approved small-molecule drug substances containing fluorine (and the lack of spectral interferences due to the absence of fluorine in pharmaceutical excipients), we expect ^{19}F-based methods for probing molecular packing to be widely applicable to structural determination of fluorine-containing APIs in both crystalline and amorphous forms in drug substances and products.

5. Conclusion

We present a ssNMR investigation of molecular packing in crystalline and amorphous materials using POSA as a model system and obtain comprehensive details on the microstructure and local order of amorphous solids. A combination of high-resolution 1D and 2D hetero-nuclear ssNMR experiments reports semi-quantitatively the structural differences between crystalline and amorphous POSA. Particularly, ^{19}F-^{19}F, ^{1}H-^{19}F and ^{13}C-^{19}F correlation techniques identify site-specific intra- and inter-molecular contacts for uncovering high resolution details. Moreover, ^{13}C-^{19}F REDOR provides atomic distance measurements for further refinement of the packing model in amorphous POSA. Our study has proposed likely the first atomic-level structural model of local "head-to-tail" packing in amorphous pharmaceuticals by taking POSA as an example. We provide structural details for a fundamental understanding of molecular packing change in the crystalline-to-amorphous interconversion. The MAS NMR method presented in this work will open new avenues for molecular understanding of amorphous materials and its correlation with functions and properties.

6. Acknowledgment

X. L. and M. L. are grateful to MRL Postdoctoral Research Program. L. Y. acknowledges NSF support through the University of Wisconsin Materials Research Science and Engineering Center (Grant DMR-1720415). The authors appreciate the insightful discussions with Drs. Luke Schenck, Aaron Cote, Andrew Brunskill, Dirk Stueber, and Narayan Variankaval at MRLs, Merck & Co., Inc. (Kenilworth, NJ 07033, US).

7. References

1. Blagden, N.; de Matas, M.; Gavan, P. T.; York, P. Crystal engineering of active pharmaceutical ingredients to improve solubility and dissolution rates. *Adv. Drug Del. Rev.* **2007,** *59* (7), 617-630.
2. Yu, L. Amorphous pharmaceutical solids: Preparation, characterization and stabilization. *Adv. Drug Del. Rev.* **2001,** *48* (1), 27-42.
3. Giri, G.; Park, S.; Vosgueritchian, M.; Shulaker, M. M.; Bao, Z. High-mobility, aligned crystalline domains of tips-pentacene with metastable polymorphs through lateral confinement of crystal growth. *Adv. Mater.* **2014,** *26* (3), 487-493.
4. Shirota, Y. Photo- and electroactive amorphous molecular materials—molecular design, syntheses, reactions, properties, and applications. *J. Mater. Chem.* **2005,** *15* (1), 75-93.
5. Bauer, J.; Spanton, S.; Henry, R.; Quick, J.; Dziki, W.; Porter, W.; Morris, J. Ritonavir: An extraordinary example of conformational polymorphism. *Pharm. Res.* **2001,** *18* (6), 859-866.
6. Paudel, A.; Geppi, M.; Mooter, G. V. D. Structural and dynamic properties of amorphous solid dispersions: The role of solid-state nuclear magnetic resonance spectroscopy and relaxometry. *J. Pharm. Sci.* **2014,** *103* (9), 2635-2662.
7. Mishima, O.; Suzuki, Y. Propagation of the polyamorphic transition of ice and the liquid–liquid critical point. *Nature* **2002,** *419* (6907), 599-603.
8. Ha, A.; Cohen, I.; Zhao, X.; Lee, M.; Kivelson, D. Supercooled liquids and polyamorphism. *J. Phys. Chem.* **1996,** *100* (1), 1-4.
9. Kurita, R.; Tanaka, H. On the abundance and general nature of the liquid–liquid phase transition in molecular systems. *J. Phys.: Condens. Matter* **2005,** *17* (27), L293-L302.
10. Zhu, M.; Wang, J.-Q.; Perepezko, J. H.; Yu, L. Possible existence of two amorphous phases of d-mannitol related by a first-order transition. *The Journal of Chemical Physics* **2015,** *142* (24), 244504.
11. Zhu, M.; Yu, L. Polyamorphism of d-mannitol. *J. Chem. Phys.* **2017,** *146* (24), 244503.
12. Rumondor, A. C. F.; Wikström, H.; Van Eerdenbrugh, B.; Taylor, L. S. Understanding the tendency of amorphous solid dispersions to undergo amorphous–amorphous phase separation in the presence of absorbed moisture. *AAPS PharmSciTech* **2011,** *12* (4), 1209-1219.
13. Benmore, C. J.; Weber, J. K. R.; Tailor, A. N.; Cherry, B. R.; Yarger, J. L.; Mou, Q.; Weber, W.; Neuefeind, J.; Byrn, S. R. Structural characterization and aging of glassy pharmaceuticals made using acoustic levitation. *J. Pharm. Sci.* **2013,** *102* (4), 1290-1300.
14. Dempah, K. E.; Barich, D. H.; Kaushal, A. M.; Zong, Z.; Desai, S. D.; Suryanarayanan, R.; Kirsch, L.; Munson, E. J. Investigating gabapentin polymorphism using solid-state NMR spectroscopy. *AAPS PharmSciTech* **2013,** *14* (1), 19-28.
15. Yang, F.; Su, Y.; Zhu, L.; Brown, C. D.; Rosen, L. A.; Rosenberg, K. J. Rheological and solid-state NMR assessments of copovidone/clotrimazole model solid dispersions. *Int. J. Pharm.* **2016,** *500* (1-2), 20-31.
16. Ni, Q. Z.; Yang, F.; Can, T. V.; Sergeyev, I. V.; D'Addio, S. M.; Jawla, S. K.; Li, Y.; Lipert, M. P.; Xu, W.; Williamson, R. T.; Leone, A.; Griffin, R. G.; Su, Y. In situ characterization of pharmaceutical formulations by dynamic nuclear polarization enhanced MAS NMR. *J. Phys. Chem. B* **2017,** *121* (34), 8132-8141.

17. Yuan, X.; Xiang, T. X.; Anderson, B. D.; Munson, E. J. Hydrogen bonding interactions in amorphous indomethacin and its amorphous solid dispersions with poly(vinylpyrrolidone) and poly(vinylpyrrolidone-co-vinyl acetate) studied using (13)C solid-state NMR. *Mol. Pharm.* **2015,** *12* (12), 4518-28.
18. Zhao, L.; Hanrahan, M. P.; Chakravarty, P.; DiPasquale, A. G.; Sirois, L. E.; Nagapudi, K.; Lubach, J. W.; Rossini, A. J. Characterization of pharmaceutical cocrystals and salts by dynamic nuclear polarization-enhanced solid-state NMR spectroscopy. *Crystal Growth & Design* **2018,** *18* (4), 2588-2601.
19. Vogt, F. G. Characterization of pharmaceutical compounds by solid-state NMR. *Emagres* **2015,** *4* (2), 255-268.
20. Paradowska, K.; Wawer, I. Solid-state NMR in the analysis of drugs and naturally occurring materials. *J. Pharm. Biomed. Anal.* **2014,** *93*, 27-42.
21. Veinberg, S. L.; Johnston, K. E.; Jaroszewicz, M. J.; Kispal, B. M.; Mireault, C. R.; Kobayashi, T.; Pruski, M.; Schurko, R. W. Natural abundance N-14 and N-15 solid-state NMR of pharmaceuticals and their polymorphs. *PCCP* **2016,** *18* (26), 17713-17730.
22. Policianova, O.; Urbanova, M.; Kobera, L.; Brus, J. Solid-state NMR characterization of solid dispersions of drugs in polymer matrices by NMR spectroscopy. *Chem. Listy* **2013,** *107* (10), 761-768.
23. Skorupska, E.; Jeziorna, A.; Kazmierski, S.; Potrzebowski, M. J. Recent progress in solid-state NMR studies of drugs confined within drug delivery systems. *Solid State Nucl. Magn. Reson.* **2014,** *57-58*, 2-16.
24. Lu, X.; Xu, W.; Hanada, M.; Jermain, S. V.; Williams, R. O., 3rd; Su, Y. Solid-state NMR analysis of crystalline and amorphous indomethacin: An experimental protocol for full resonance assignments. *J. Pharm. Biomed. Anal.* **2019,** *165*, 47-55.
25. Martineau, C. NMR crystallography: Applications to inorganic materials. *Solid State Nucl. Magn. Reson.* **2014,** *63-64*, 1-12.
26. Bryce, D. L.; Taulelle, F. NMR crystallography. *Acta Crystallogr C Struct Chem* **2017,** *73* (Pt 3), 126-127.
27. Greenwood, A. I.; Clay, M. C.; Rienstra, C. M. 31P-dephased, 13C-detected redor for NMR crystallography at natural isotopic abundance. *J. Magn. Reson.* **2017,** *278*, 8-17.
28. Giovine, R.; Volkringer, C.; Trebosc, J.; Amoureux, J. P.; Loiseau, T.; Lafon, O.; Pourpoint, F. NMR crystallography to probe the breathing effect of the mil-53(Al) metal-organic framework using solid-state NMR measurements of 13C-27Al distances. *Acta Crystallogr C Struct Chem* **2017,** *73* (Pt 3), 176-183.
29. Mesch, M. B.; Barwinkel, K.; Krysiak, Y.; Martineau, C.; Taulelle, F.; Neder, R. B.; Kolb, U.; Senker, J. Solving the hydrogen and lithium substructure of poly(triazine imide)/licl using NMR crystallography. *Chemistry (Easton)* **2016,** *22* (47), 16878-16890.
30. Caulkins, B. G.; Young, R. P.; Kudla, R. A.; Yang, C.; Bittbauer, T. J.; Bastin, B.; Hilario, E.; Fan, L.; Marsella, M. J.; Dunn, M. F.; Mueller, L. J. NMR crystallography of a carbanionic intermediate in tryptophan synthase: Chemical structure, tautomerization, and reaction specificity. *J. Am. Chem. Soc.* **2016,** *138* (46), 15214-15226.
31. Bouchevreau, B.; Martineau, C.; Mellot-Draznieks, C.; Dutour, J.; Tuel, A.; Suchomel, M. R.; Trebosc, J.; Lafon, O.; Amoureux, J. P.; Taulelle, F. Corrigendum: An NMR-driven crystallography strategy to overcome the computability limit of powder structure determination: A layered aluminophosphate case. *Chemistry (Easton)* **2016,** *22* (36), 12588.
32. Marker, K.; Pingret, M.; Mouesca, J. M.; Gasparutto, D.; Hediger, S.; De Paepe, G. A new tool for NMR crystallography: Complete (13)C/(15)N assignment of organic molecules at natural isotopic abundance using dnp-enhanced solid-state NMR. *J. Am. Chem. Soc.* **2015,** *137* (43), 13796-9.
33. Baias, M.; Dumez, J. N.; Svensson, P. H.; Schantz, S.; Day, G. M.; Emsley, L. De novo determination of the crystal structure of a large drug molecule by crystal structure prediction-based powder NMR crystallography. *J. Am. Chem. Soc.* **2013,** *135* (46), 17501-7.
34. Luchinat, C.; Parigi, G.; Ravera, E.; Rinaldelli, M. Solid-state NMR crystallography through paramagnetic restraints. *J. Am. Chem. Soc.* **2012,** *134* (11), 5006-9.

35. Davies, E.; Duer, M. J.; Ashbrook, S. E.; Griffin, J. M. Applications of NMR crystallography to problems in biomineralization: Refinement of the crystal structure and 31P solid-state NMR spectral assignment of octacalcium phosphate. *J. Am. Chem. Soc.* **2012,** *134* (30), 12508-15.
36. Salager, E.; Day, G. M.; Stein, R. S.; Pickard, C. J.; Elena, B.; Emsley, L. Powder crystallography by combined crystal structure prediction and high-resolution 1H solid-state NMR spectroscopy. *J. Am. Chem. Soc.* **2010,** *132* (8), 2564-6.
37. Elena, B.; Pintacuda, G.; Mifsud, N.; Emsley, L. Molecular structure determination in powders by NMR crystallography from proton spin diffusion. *J. Am. Chem. Soc.* **2006,** *128* (29), 9555-60.
38. Elena, B.; Emsley, L. Powder crystallography by proton solid-state NMR spectroscopy. *J. Am. Chem. Soc.* **2005,** *127* (25), 9140-6.
39. Middleton, D. A.; Le Duff, C. S.; Peng, X.; Reid, D. G.; Saunders, D. Molecular conformations of the polymorphic forms of cimetidine from C-13 solid-state NMR distance and angle measurements. *J. Am. Chem. Soc.* **2000,** *122* (6), 1161-1170.
40. Harper, J. K.; Grant, D. M.; Zhang, Y. G.; Lee, P. L.; Von Dreele, R. Characterizing challenging microcrystalline solids with solid-state NMR shift tensor and synchrotron X-ray powder diffraction data: Structural analysis of ambuic acid. *J. Am. Chem. Soc.* **2006,** *128* (5), 1547-1552.
41. Harper, J. K.; Iuliucci, R.; Gruber, M.; Kalakewich, K. Refining crystal structures with experimental C-13 NMR shift tensors and lattice-including electronic structure methods. *Crystengcomm* **2013,** *15* (43), 8693-8704.
42. Kalakewich, K.; Iuliucci, R.; Harper, J. K. Establishing accurate high-resolution crystal structures in the absence of diffraction data and single crystals-an NMR approach. *Crystal Growth & Design* **2013,** *13* (12), 5391-5396.
43. Kalakewich, K.; Iuliucci, R.; Mueller, K. T.; Eloranta, H.; Harper, J. K. Monitoring the refinement of crystal structures with N-15 solid-state NMR shift tensor data. *J. Chem. Phys.* **2015,** *143* (19).
44. Soss, S. E.; Flynn, P. F.; Iuliucci, R. J.; Young, R. P.; Mueller, L. J.; Hartman, J.; Beran, G. J. O.; Harper, J. K. Measuring and modeling highly accurate N-15 chemical shift tensors in a peptide. *Chemphyschem* **2017,** *18* (16), 2225-2232.
45. Ashbrook, S. E.; McKay, D. Combining solid-state NMR spectroscopy with first-principles calculations - a guide to NMR crystallography. *Chem. Commun. (Camb.)* **2016,** *52* (45), 7186-204.
46. Widdifield, C. M.; Perras, F. A.; Bryce, D. L. Solid-state (185/187)Re NMR and gipaw dft study of perrhenates and re2(co)10: Chemical shift anisotropy, NMR crystallography, and a metal-metal bond. *Phys. Chem. Chem. Phys.* **2015,** *17* (15), 10118-34.
47. Pourpoint, F.; Yehl, J.; Li, M.; Gupta, R.; Trebosc, J.; Lafon, O.; Amoureux, J. P.; Polenova, T. NMR crystallography of an oxovanadium(v) complex by an approach combining multinuclear magic angle spinning NMR, dft, and spin dynamics simulations. *Chemphyschem* **2015,** *16* (8), 1619-26.
48. Pickard, C. J.; Salager, E.; Pintacuda, G.; Elena, B.; Emsley, L. Resolving structures from powders by NMR crystallography using combined proton spin diffusion and plane wave dft calculations. *J. Am. Chem. Soc.* **2007,** *129* (29), 8932-3.
49. Hofstetter, A.; Emsley, L. Positional variance in NMR crystallography. *J. Am. Chem. Soc.* **2017,** *139* (7), 2573-2576.
50. Day, G. M.; WD, S. M.; Jones, W. A strategy for predicting the crystal structures of flexible molecules: The polymorphism of phenobarbital. *Phys. Chem. Chem. Phys.* **2007,** *9* (14), 1693-704.
51. Bradley, J. P.; Velaga, S. P.; Antzutkin, O. N.; Brown, S. P. Probing intermolecular crystal packing in γ-indomethacin by high-resolution 1H solid-state NMR spectroscopy. *Crystal Growth & Design* **2011,** *11* (8), 3463-3471.
52. Poppler, A. C.; Corlett, E. K.; Pearce, H.; Seymour, M. P.; Reid, M.; Montgomery, M. G.; Brown, S. P. Single-crystal x-ray diffraction and NMR crystallography of a 1:1 cocrystal of dithianon and pyrimethanil. *Acta Crystallogr C Struct Chem* **2017,** *73* (Pt 3), 149-156.
53. Macholl, S.; Borner, F.; Buntkowsky, G. Revealing the configuration and crystal packing of organic compounds by solid-state NMR spectroscopy: Methoxycarbonylurea, a case study. *Chemistry (Easton)* **2004,** *10* (19), 4808-16.

54. Madine, J.; Middleton, D. A. An NMR strategy for obtaining multiple conformational constraints for 15n-13c spin-pair labelled organic solids. *Phys. Chem. Chem. Phys.* **2006,** *8* (44), 5223-8.
55. Gullion, T.; Schaefer, J. Rotational-echo double-resonance NMR. *J Magn Reson 1989* **1989,** *81* (1), 196-200.
56. Barry, S. J.; Pham, T. N.; Borman, P. J.; Edwards, A. J.; Watson, S. A. A risk-based statistical investigation of the quantification of polymorphic purity of a pharmaceutical candidate by solid-state 19f NMR. *Anal. Chim. Acta* **2012,** *712*, 30-6.
57. Huang, C.; Klinzing, G.; Procopio, A.; Yang, F.; Ren, J.; Burlage, R.; Zhu, L.; Su, Y. Understanding compression-induced amorphization of crystalline posaconazole. *Mol. Pharm.* **2019,** *16* (2), 825-833.
58. Urbanova, M.; Brus, J.; Sedenkova, I.; Policianova, O.; Kobera, L. Characterization of solid polymer dispersions of active pharmaceutical ingredients by 19F MAS NMR and factor analysis. *Spectrochim. Acta. A Mol. Biomol. Spectrosc.* **2013,** *100*, 59-66.
59. Lu, X.; Huang, C.; Lowinger, M. B.; Yang, F.; Xu, W.; Brown, C. D.; Hesk, D.; Koynov, A.; Schenck, L.; Su, Y. Molecular interactions in posaconazole amorphous solid dispersions from two-dimensional solid-state NMR spectroscopy. *Mol. Pharm.* **2019,** *16* (6), 2579-2589.
60. Aso, Y.; Yoshioka, S.; Miyazaki, T.; Kawanishi, T. Feasibility of 19F-NMR for assessing the molecular mobility of flufenamic acid in solid dispersions. *Chem. Pharm. Bull. (Tokyo)* **2009,** *57* (1), 61-4.
61. Aimi, K.; Ando, S. Conformation analysis and molecular mobility of ethylene and tetrafluoroethylene copolymer using solid-state 19F MAS and 1H --> 19F CP/MAS NMR spectroscopy. *Magn. Reson. Chem.* **2004,** *42* (7), 577-88.
62. Matsumori, N.; Kasai, Y.; Oishi, T.; Murata, M.; Nomura, K. Orientation of fluorinated cholesterol in lipid bilayers analyzed by 19F tensor calculation and solid-state NMR. *J. Am. Chem. Soc.* **2008,** *130* (14), 4757-66.
63. Brinkmann, A.; Sternberg, U.; Bovee-Geurts, P. H. M.; Fernandez Fernandez, I.; Lugtenburg, J.; Kentgens, A. P. M.; DeGrip, W. J. Insight into the chromophore of rhodopsin and its meta-ii photointermediate by (19)F solid-state NMR and chemical shift tensor calculations. *Phys. Chem. Chem. Phys.* **2018,** *20* (48), 30174-30188.
64. Szell, P. M.; Gabriel, S. A.; Gill, R. D.; Wan, S. Y.; Gabidullin, B.; Bryce, D. L. (13)C and (19)F solid-state NMR and x-ray crystallographic study of halogen-bonded frameworks featuring nitrogen-containing heterocycles. *Acta Crystallogr C Struct Chem* **2017,** *73* (Pt 3), 157-167.
65. Goossens, P.; Martineau-Corcos, C.; Saidi, F.; Martens, J. A.; Taulelle, F. Unlocking the observation of different proton populations in fluorinated polymers by solid-state (1)H and (19)F double resonance NMR spectroscopy. *Phys. Chem. Chem. Phys.* **2016,** *18* (41), 28726-28731.
66. Giraudet, J.; Dubois, M.; Hamwi, A.; Stone, W. E.; Pirotte, P.; MASin, F. Solid-state NMR (19F and 13C) study of graphite monofluoride (cf)n: 19F spin-lattice magnetic relaxation and 19F/13C distance determination by hartmann-hahn cross polarization. *J. Phys. Chem. B* **2005,** *109* (1), 175-81.
67. Wenslow, R. M. 19F solid-state NMR spectroscopic investigation of crystalline and amorphous forms of a selective muscarinic M3 receptor antagonist, in both bulk and pharmaceutical dosage form samples. *Drug Dev. Ind. Pharm.* **2002,** *28* (5), 555-61.
68. DeVore, M. A., 2nd; Klug, C. A.; Kriz, M. R.; Roy, L. E.; Wellons, M. S. Investigations of uranyl fluoride sesquihydrate (UO2F2.1.57H2O): Combining (19)F solid-state MAS NMR spectroscopy and gipaw chemical shift calculations. *J. Phys. Chem. A* **2018,** *122* (34), 6873-6878.
69. Robbins, A. J.; Ng, W. T.; Jochym, D.; Keal, T. W.; Clark, S. J.; Tozer, D. J.; Hodgkinson, P. Combining insights from solid-state NMR and first principles calculation: Applications to the 19F NMR of octafluoronaphthalene. *Phys. Chem. Chem. Phys.* **2007,** *9* (19), 2389-96.
70. Abraham, A.; Crull, G. Understanding api-polymer proximities in amorphous stabilized composite drug products using fluorine-carbon 2D hetcor solid-state NMR. *Mol. Pharm.* **2014,** *11* (10), 3754-9.
71. Lu, M.; Wang, M.; Sergeyev, I. V.; Quinn, C. M.; Struppe, J.; Rosay, M.; Maas, W.; Gronenborn, A. M.; Polenova, T. (19)F dynamic nuclear polarization at fast magic angle spinning for NMR of HIV-1 capsid protein assemblies. *J. Am. Chem. Soc.* **2019,** *141* (14), 5681-5691.

72. Wang, M.; Lu, M.; Fritz, M. P.; Quinn, C. M.; Byeon, I. J. L.; Byeon, C. H.; Struppe, J.; Maas, W.; Gronenborn, A. M.; Polenova, T. Fast magic-angle spinning F-19 NMR spectroscopy of HIV-1 capsid protein assemblies. *Angewandte Chemie-International Edition* **2018,** *57* (50), 16375-16379.
73. Wi, S.; Sinha, N.; Hong, M. Long-range 1H-19F distance measurement in peptides by solid-state NMR. *J. Am. Chem. Soc.* **2004,** *126* (40), 12754-5.
74. Mani, R.; Cady, S. D.; Tang, M.; Waring, A. J.; Lehrer, R. I.; Hong, M. Membrane-dependent oligomeric structure and pore formation of a beta-hairpin antimicrobial peptide in lipid bilayers from solid-state NMR. *Proc. Natl. Acad. Sci. U. S. A.* **2006,** *103* (44), 16242-7.
75. Goetz, J. M.; Poliks, B.; Studelska, D. R.; Fischer, M.; Kugelbrey, K.; Bacher, A.; Cushman, M.; Schaefer, J. Investigation of the binding of fluorolumazines to the 1-mda capsid of lumazine synthase by N-15{F-19} redor NMR. *J. Am. Chem. Soc.* **1999,** *121* (33), 7500-7508.
76. Shcherbakov, A. A.; Hong, M. Rapid measurement of long-range distances in proteins by multidimensional (13)C-(19)F redor NMR under fast magic-angle spinning. *J. Biomol. NMR* **2018,** *71* (1), 31-43.
77. Gomez, J.; Gujral, A.; Huang, C. B.; Bishop, C.; Yu, L.; Ediger, M. D. Nematic-like stable glasses without equilibrium liquid crystal phases. *J. Chem. Phys.* **2017,** *146* (5).
78. Bishop, C.; Thelen, J. L.; Gann, E.; Toney, M. F.; Yu, L.; DeLongchamp, D. M.; Ediger, M. D. Vapor deposition of a nonmesogen prepares highly structured organic glasses. *Proc. Natl. Acad. Sci. U. S. A.* **2019,** *116* (43), 21421-21426.
79. Wu, X. L.; Burns, S. T.; Zilm, K. W. Spectral editing in cpMAS NMR - generating subspectra based on proton multiplicities. *J. Magn. Reson., Ser A* **1994,** *111* (1), 29-36.
80. Martin, G. E. Posaconazole: Application of hsqc-adequate from general indirect covariance processing. *J. Heterocycl. Chem.* **2012,** *49* (3), 716-720.
81. McQuiston, D. K.; Mucalo, M. R.; Saunders, G. C. The structure of posaconazole and its solvates with methanol, and dioxane and water: Difluorophenyl as a hydrogen bond donor. *J. Mol. Struct.* **2019,** *1179*, 477-486.
82. Shcherbakov, A. A.; Roos, M.; Kwon, B.; Hong, M. Two-dimensional (19)F-(13)C correlation NMR for (19)F resonance assignment of fluorinated proteins. *J. Biomol. NMR* **2020**.
83. Liang, L.; Hou, G.; Bao, X. Measurement of proton chemical shift anisotropy in solid-state NMR spectroscopy. *Solid State Nucl. Magn. Reson.* **2018,** *93*, 16-28.
84. Hou, G.; ParaMASivam, S.; Yan, S.; Polenova, T.; Vega, A. J. Multidimensional magic angle spinning NMR spectroscopy for site-resolved measurement of proton chemical shift anisotropy in biological solids. *J. Am. Chem. Soc.* **2013,** *135* (4), 1358-68.
85. Lu, M.; Sarkar, S.; Wang, M.; Kraus, J.; Fritz, M.; Quinn, C. M.; Bai, S.; Holmes, S. T.; Dybowski, C.; Yap, G. P. A.; Struppe, J.; Sergeyev, I. V.; Maas, W.; Gronenborn, A. M.; Polenova, T. 19F magic angle spinning NMR spectroscopy and density functional theory calculations of fluorosubstituted tryptophans: Integrating experiment and theory for accurate determination of chemical shift tensors. *The Journal of Physical Chemistry B* **2018,** *122* (23), 6148-6155.
86. Etter, M. C. Encoding and decoding hydrogen-bond patterns of organic-compounds. *Acc. Chem. Res.* **1990,** *23* (4), 120-126.
87. Kothari, K.; Ragoonanan, V.; Suryanarayanan, R. The role of drug–polymer hydrogen bonding interactions on the molecular mobility and physical stability of nifedipine solid dispersions. *Mol. Pharm.* **2015,** *12* (1), 162-170.
88. Mistry, P.; Mohapatra, S.; Gopinath, T.; Vogt, F. G.; Suryanarayanan, R. Role of the strength of drug-polymer interactions on the molecular mobility and crystallization inhibition in ketoconazole solid dispersions. *Mol. Pharm.* **2015,** *12* (9), 3339-50.
89. Tatton, A. S.; Pham, T. N.; Vogt, F. G.; Iuga, D.; Edwards, A. J.; Brown, S. P. Probing hydrogen bonding in cocrystals and amorphous dispersions using (14)N-(1)H hmqc solid-state NMR. *Mol. Pharm.* **2013,** *10* (3), 999-1007.
90. Su, Y.; Andreas, L.; Griffin, R. G. Magic angle spinning NMR of proteins: High-frequency dynamic nuclear polarization and (1)h detection. *Annu. Rev. Biochem.* **2015,** *84*, 465-97.

91. Viger-Gravel, J.; Avalos, C. E.; Kubicki, D. J.; Gajan, D.; Lelli, M.; Ouari, O.; Lesage, A.; Emsley, L. (19) f magic angle spinning dynamic nuclear polarization enhanced NMR spectroscopy. *Angew. Chem. Int. Ed. Engl.* **2019,** *58* (22), 7249-7253.
92. Lu, X.; Skomski, D.; Thompson, K. C.; McNevin, M. J.; Xu, W.; Su, Y. Three-dimensional NMR spectroscopy of fluorinated pharmaceutical solids under ultrafast magic angle spinning. *Anal. Chem.* **2019,** *91* (9), 6217-6224.